

# Statistical Model of Exotic Rotational Correlations in Emergent Space-Time

Craig Hogan

*University of Chicago and Fermilab*

Ohkyung Kwon<sup>a</sup>

*Korea Advanced Institute of Science and Technology*

Jonathan Richardson

*University of Chicago and University of Michigan*

A Lorentz invariant statistical model is presented for rotational fluctuations in the local inertial frame that arise from new quantum degrees of freedom of space-time. The model assumes invariant classical causal structure, and a Planck information density in invariant proper time determined by the world line of an observer. It describes macroscopic spacelike correlations that appear as observable timelike correlations in phase differences of light propagating on paths that begin and end on the same world line. The model allows an exact prediction for the autocorrelation of any interferometer time signal from the shape of the light paths. Specific examples computed for configurations that approximate realistic experiments show that the model can be rigorously tested, allowing a direct experimental probe of Planck scale degrees of freedom.

## I. INTRODUCTION

In both classical special relativity and quantum mechanics, a physical rotation, or rate of change of direction, has a definite physical meaning even on infinitesimal scales. The “local inertial frame” is an absolute and determinate physical attribute of space, measurable for example by an absence of centrifugal acceleration. However, when quantum mechanics is combined with general relativity, the use of a classical local inertial frame as a reference to define rotation becomes inconsistent, even in a flat space-time background. Because of gravitational frame dragging, space itself inherits the quantum indeterminacy of any apparatus used to measure rotation, an effect that becomes more pronounced on short time and length scales. Extrapolation of standard quantum principles[1] suggests that rotational observables of space-time are quantized at the Planck length  $l_P \equiv \sqrt{\hbar G/c^3} = 1.616 \times 10^{-35}$  meters, where a single quantum has the energy and angular momentum of a maximally rotating black hole. As in any quantum system, the quantization of space-time rotation should manifest as new forms of correlations in rotational observables. We call these “exotic” rotational correlations because they are not part of a standard quantum system of particles or fields, but arise from quantum degrees of freedom that give rise to space and time. If they could be measured, they would provide experimental clues to the nature of those degrees of freedom.

In this paper, we develop a statistical model to predict the properties of exotic rotational correlations in systems much larger than the Planck length. A purely rotational structure of correlations in space and time is fixed by the Lorentz invariant classical causal structure, with a normalization fixed by a Planck scale information density in invariant proper time. The finite information in the system leads to exotic fluctuations in measurements of rotation based on the propagation of light. In an interferometer, exotic spacelike correlations lead to exact predictions for timelike correlations of signals that depend only on the spatial layout of the light paths in space and the Planck scale information density. The model thus presents a definite, quantitative hypothesis for how inertial frames, rotation and directionality emerge statistically from quantum geometry.

Our model is embedded in a flat, classically stationary space-time, but its correlations on large scales match the Planck scale holographic information density on causal diamond surfaces required for emergent theories of gravity[2–4]. It is natural to conjecture that the specific exotic rotational degrees of freedom identified in our model describe the ground state of the quantum system that, when excited, gives rise to fully dynamical quantum gravity[5–7]. If this conjecture is correct, it may be possible to study some symmetries of quantum gravity with precision laboratory measurements.

Our analysis will be useful to design and interpret experiments based on correlations in interferometer signals, which now attain the sensitivity needed[8] to measure the predicted exotic correlation. As in previous estimates of holographic geometrical fluctuations with similar displacement magnitude[9–14], directions in this model on scale  $R$  fluctuate on timescale  $\approx R/c$ , with a variance of about  $\langle \Delta\theta^2 \rangle_R \approx l_P/R$ , which leads to a signal with a power spectral density of fractional displacement noise about equal to a Planck time[8]. However, purely rotational fluctuations would

---

<sup>a</sup> E-mail: o.kwon@kaist.ac.kr

not have been detected in current experiments that constrain holographic fluctuations with this sensitivity[15], due to their purely radial light paths. As shown below, a definitive signature of rotational correlations can be measured using modified experimental configurations.

Our model provides a concrete, quantitative example of how Planck scale departures from a classical space-time might produce detectable physical effects on much larger scales, due to large scale correlations implied by holographic information bounds. This specific model can be definitively tested with experiments, but it may not be unique: the effects of geometrical correlations on quantum states of light and matter in an apparatus are not all rigorously constrained by known basic principles. Ultimately, the best hope is that the symmetries of Planck scale geometry and their relationships to the quantum states of Standard Model fields can be probed by a systematic experimental program involving a variety of instruments, including other forms of interferometry capable of measuring superluminally time-resolved correlations with Planck sensitivity. If exotic rotational geometrical fluctuations in any form are shown to exist in laboratory experiments, they are also likely to play an important role in shaping other physical systems, such as the cosmological constant in an emergent metric with a matter field vacuum[1], or the generation of large scale metric fluctuations during an inflationary period in the early universe. Such effects depend on entanglement of the geometrical system with field vacuum states, and the back reaction on the emergent metric, which lie beyond the scope of the model developed here.

## II. EXOTIC ROTATIONAL CORRELATIONS

### A. Statistical Lorentz Invariance and Observables

A widely known difficulty in quantizing gravity is preserving local Lorentz invariance. Our model is motivated by quantum gravitational considerations, but we do not quantize gravity here, so our task is considerably easier. The model is constructed in a special relativistic space-time, in the limit of a fixed causal structure with no curvature or dynamics. The correlations are defined by spacelike displacements on light cones, which are invariant structures. Our calculated examples assume a nonaccelerating observer for realism and convenience, but since the framework depends only on invariant causal structure, it generalizes to any timelike observer.

Thus, the model preserves the principle of Lorentz invariance in a statistical sense[1]. Quantum mechanics can only make predictions about correlations, that is, statistical outcomes of measurements. We abandon the classical notion of an observer-independent, determinate and absolute space-time, but require that the correlations predicted by the theory do not depend on arbitrary choices of coordinates or frames. This property is built in by construction: the correlations in our model depend only on invariant classical causal structures.

The invariant causal structures are anchored to the specific world line of a measurement, identified as the quantum-mechanical “observer.” On this world line, we posit that proper time intervals— Lorentz scalars, invariantly and locally definable— are quantized at the Planck scale. By imposing the Planck scale information density in proper time of a measurement, we avoid the Lorentz invariance violation that occurs from a Planck scale imposed on timelike or spacelike intervals that depend on a choice of coordinate system.

Our predictions are given in terms of locally measurable observables. We present here observable statistics about correlations in proper time and frequency. Any pair of events viewed in any frame (boosted relative to the observer, say) is separated by the same invariant interval, so the predictions are invariant Lorentz scalars. The calculation involves quantities that depend on the observer’s nonlocal positional relationships with other trajectories, but begins and ends with Lorentz scalars.

### B. Model assumptions

The model is based on two principal assumptions:

1. The system has a Planck scale information density, in invariant proper time, on the world line of a measurement. Unlike a classical world line, the information content or bandwidth of a world line, and any measurement, is limited to that of a discrete 1D time series with steps of duration  $\approx l_P/c$  in invariant proper time. That limit applies as well to the rotational relationship of its local inertial frame with rest of the universe. The information available to describe directional orientation relative to an interval on a world line matches its duration in Planck units.
2. The quantum departure from a classical space-time can be represented by random Planck scale spacelike displacements that exactly preserve classical causal structure defined by the light cones of the world line of the measurement.

The exotic degrees of freedom are assumed to act physically as random Planck scale transverse position displacements of events. The displacements have zero mean fixed by the classical limit, and a nonzero variance from quantum fluctuations. They are not independent, but must be highly correlated within a Planck time, because of the Planck information density. Correlations in a measurement are determined by the invariant light cones of a measurement interval. Because of the limited information in any finite interval, measurements of rotation fluctuate from the absolute classical inertial frame. While null relationships between events are exactly preserved, timelike and spacelike relationships depend on preparation and measurement of a state.

These are the only properties of the quantum geometry necessary to specify the exotic statistical effects on propagating light in flat space-time. The Planck scale normalization is fixed by requiring that the number of degrees of freedom of a causal diamond agrees with holographic gravity. The system approaches a standard, flat space-time on scales much larger than the Planck length, in a nontrivial way that is uniquely fixed by these assumptions. The model accounts for how a nearly classical inertial frame around any world line emerges over a long time interval from indeterminate rotation at the Planck scale.

### C. Covariance of Random Displacement on Future Light Cones of an Observer

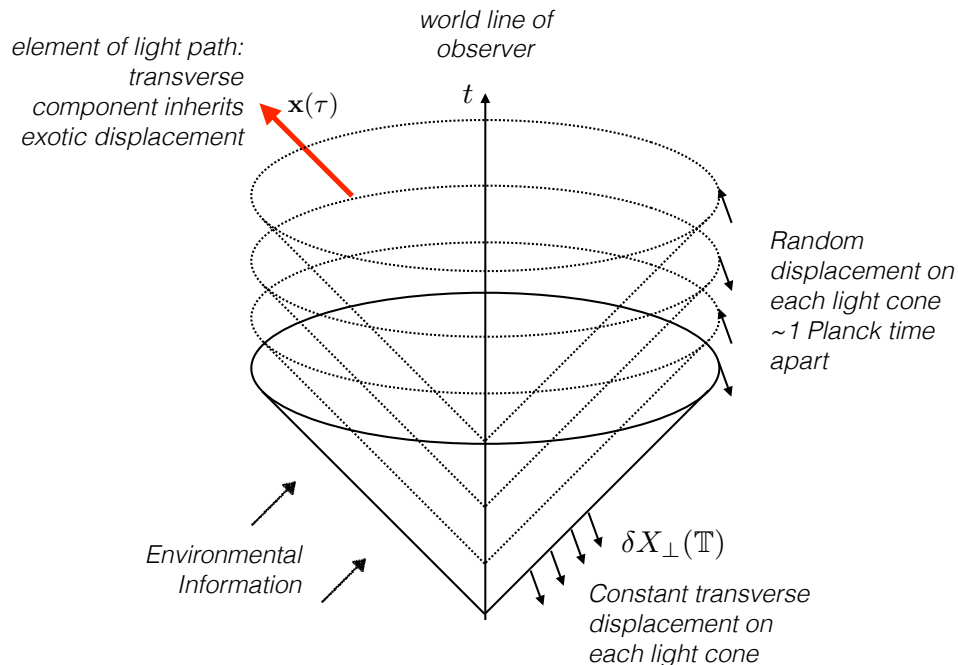


FIG. 1. Classical picture of the causal structure of large scale covariances in exotic space-time positional relationships. Space and time are shown in the observer’s frame, with one spatial dimension suppressed. A series of light cones, surfaces of constant light cone time  $\mathbb{T}$ , is shown emerging from an observer’s world line. These determine the space-time structure of correlations produced by Planck scale entanglement. Within a Planck length of each surface of constant  $\mathbb{T}$ , the same random transverse spatial displacement or “quantum twist”  $\delta X_{\perp}(\mathbb{T})$  of about a Planck length— a consequence of noncommutative geometry at the Planck scale— is causally inherited by entanglement with a quantum state prepared on the observer’s world line. Thus, entanglement is causally local: each event on the observer’s world line determines the projection of all future events that lie within a Planck length of null separation. Propagating light inherits the projection of the local transverse displacement onto its path  $\mathbf{x}(\tau)$ . The total effect on the light phase is an accumulation of projected components of random displacements from crossing a series of light cones. Transverse displacements accumulate like a random walk and lead to a mean square displacement much larger than the Planck length.

Light cones (or null cones) are the covariant objects that define causal structure: they define the sharp classical boundaries between past, present and future, and between timelike and spacelike separation of events. We base our

model on the principle that classical causal structure is respected on all scales larger than the Planck length. In the frame of an observer  $O$ , we define a “light cone time” coordinate variable,

$$\mathbb{T}_O = t_O - \frac{|\mathbf{x}_O|}{c}. \quad (1)$$

A surface of constant  $\mathbb{T}$  in 3+1D represents a 2+1D light cone emanating from an event on an observer’s world line, a 3-surface defined in conventional coordinates by  $t = |\mathbf{x}|/c$ . Although we will choose to calculate in the rest frame of an observer, the causal relationships defined by the actual light cones are independent of the choice of frame and have a Lorentz invariant physical meaning. In the following, we drop subscripts until they are needed later for comparing measurements from more than one observer.

To connect with physical observables we develop a model of the geometrical character of random variables, which will allow us to compute how the random displacements affect physical quantities. The exotic departure from the classical system is described as a random variable with variance  $\ell_P^2$ :

$$\delta X_{\perp}(\mathbb{T}) \sim \mathcal{N}(0, \ell_P^2). \quad (2)$$

The transverse displacement variable  $\delta X_{\perp}$  represents an exotic displacement relative to the classical inertial frame, normal to the direction to the observer. It has zero mean so the large scale average is classical. In our model it is interpreted physically as a displacement of phase for transversely propagating light, but should be regarded as a modification of classical position of space itself, and everything in it, relative to the observer. The coherence scale and randomness model the effect of the finite information content of the indeterminate quantum elements. Since the physical effects are purely transverse, the model exactly preserves causal structure, an assumed exact symmetry of quantum gravity.

In a discrete description with the same information content, this quantity corresponds to an exotic incremental displacement at each discrete step—a random step of length  $\ell_P$  each timestep  $t_P$ , due the noncommutativity of discrete quantum geometrical operators. All of the predictions below have only one parameter,  $\ell_P$ , which, to be consistent with a discrete description and exact causal symmetry, denotes both the coherence length of the quantum elements and the magnitude of random displacements. A non-zero value of  $\ell_P$  results in a finite, countable information content, and introduces deviations from classical continuous space-time. Based on extrapolation of gravity and quantum mechanics[1, 9–14], its value should be approximately the Planck length  $l_P$ .

We now introduce the central hypothesis that encapsulates the relationship of Planck scale quantum elements to each other and to an observer on large scales (see Fig. 1). That hypothesis can be written as a covariance of an exotic displacement on future light cones:

$$\text{cov}(\delta X_{\perp}(\mathbb{T}'), \delta X_{\perp}(\mathbb{T}'')) = \begin{cases} \ell_P^2, & |\mathbb{T}'' - \mathbb{T}'| < \frac{1}{2}t_P \\ 0, & \text{otherwise} \end{cases} \quad (3)$$

For calculational convenience and clarity, in place of a discrete model of time steps, or a continuous Gaussian roll-off (say), the model uses sharply delineated bins of constant covariance in  $\mathbb{T}$ ; none of the results depend on this choice.

Although we call the displacements “quantum twists,” note that the variable represents a constant transverse displacement, and not a constant angle, everywhere on the light cone, independent of separation from the observer. The correlations that result from entanglement appear spooky, since they appear nonlocally across spacelike hypersurfaces, but they are still local in the sense that they are determined by sub-Planck light cone time separation between events. Causal relationships determine the collapse of the quantum state into classical random observables.

Although directions at the Planck length are indeterminate (and if measured, fluctuate by about a radian per Planck time), nearly classical directions emerge in a large scale average. Directions to distant objects and events are not independent, but are entangled with each other; those at distance  $R$  can be encoded by  $\approx (R/\ell_P)$  qubits. Information from each event on a world line prepares the state and entangles it with the projection of the displacement operators at all events on its light cone. Our use of a random variable is a classical shorthand for quantum decoherence, and our covariance is a classical shortcut to describe quantum entanglement among the individual Planck scale elements: events on a light cone must “agree on” the projection of the corresponding spin state onto any given axis. In the plane of an interferometer, every point on a light cone steps clockwise or counterclockwise by one Planck length from the previous one. Apparently non-local spatial correlations arise from causal entanglement of the Planck scale degrees of freedom.

It will prove further convenient to define a *rate* of transverse position fluctuation, or an effective transverse “velocity” or jitter,

$$\frac{dX_{\perp}(\mathbb{T})}{d\mathbb{T}} \equiv \frac{\delta X_{\perp}(\mathbb{T})}{t_P} \quad (4)$$

This quantity is not a physical velocity or momentum, but represents a discrete “motion” of the Planck scale quantum elements with respect to the classical system. It is explicitly dependent only on  $\mathbb{T}$  (and not individually on  $t$  or  $\mathbf{x}$ ) due to the coherence of the fluctuations on light cones. This variable is distributed as

$$\frac{dX_{\perp}(\mathbb{T})}{d\mathbb{T}} \sim \mathcal{N}\left(0, \left(\frac{\ell_P}{t_P}\right)^2\right) \quad (5)$$

with the covariance structure

$$\text{cov}\left(\frac{dX_{\perp}}{d\mathbb{T}}(\mathbb{T}'), \frac{dX_{\perp}}{d\mathbb{T}}(\mathbb{T}'')\right) = \begin{cases} \left(\frac{\ell_P}{t_P}\right)^2, & |\mathbb{T}'' - \mathbb{T}'| < \frac{1}{2}t_P \\ 0, & \text{otherwise} \end{cases} \quad (6)$$

The characteristic rate of a transverse position random walk is thus one coherence length per coherence time, or  $c$ .

### III. EXOTIC CORRELATIONS IN INTERFEROMETER SIGNALS

We now estimate the effect of exotic displacements on measurable phase shifts in beams of freely-propagating light. These phase shifts are measured by an interferometer consisting of a beamsplitter and two or more reflecting mirrors. Light from a coherent source is split into two beams which propagate through an arrangement of mirrors and back to the beamsplitter, where they recombine. Any difference in the distance propagated by the two beams introduces a corresponding difference in the accumulated optical phase. Interference effects from this phase difference modulate the power of the recombined beam, which is read out via a photodetector at the output, or antisymmetric port of the instrument. In this section, the general response of an interferometer to exotic rotational displacements will be derived. In spite of the simple and symmetric form of the fundamental exotic covariance, the projection onto observables is surprisingly subtle. These results will be used below to compute the instrument response of specific configurations of mirrors.

#### A. Effect of Exotic Displacements on the Signal

We model the effect of exotic displacements on an idealized interferometer. Propagating light encounters a beamsplitter and divides into two separate paths, 1 and 2, of equal expected length. The power at the antisymmetric port is exquisitely sensitive to the difference in path lengths[16]. A time series of measurements is represented by

$$S(t) \equiv S_2(t) - S_1(t). \quad (7)$$

Here  $S_1$  and  $S_2$  represent the optical path lengths (OPL) of the two arms and  $S$  represents the optical path difference (OPD), in the inertial frame of the beamsplitter, and  $t$  denotes laboratory time.

We now show how the exotic fluctuations manifest as random deviations from the classical OPL. The two classical optical paths will be parameterized by propagation time  $\tau \in [0, \mathcal{T}]$ , where  $\mathcal{T}$  is the full duration of the optical phase measurement, the length of each path. At propagation time  $\tau$ , the classical position of a tracer photon traversing path  $i$  will be denoted by  $\mathbf{x}_i(\tau)$ . These tracer photons do not represent actual quanta of localized energy, but rather null propagation in the inertial frame. At every point along optical path  $\mathbf{x}_{1,2}(\tau)$ , there exists a unit vector tangent to the path,  $\dot{\mathbf{x}}_{1,2}(\tau)/c \equiv d\mathbf{x}_{1,2}(\tau)/cd\tau$ . This unit vector represents the instantaneous direction of light travel through interferometer.

The light origin,  $\mathbf{x}_1(0) = \mathbf{x}_2(0)$ , provides a common reference for the optical phase measurement made by either path. It can thus be regarded, under a relational theory, as a fixed reference point against which all other points in space appear to fluctuate. For each path, the optical distance propagated by the tracer photon over a classical light-crossing time is given by the path integral

$$S_{1,2}(t + \mathcal{T}) = \int_t^{t+\mathcal{T}} \left[ \dot{\mathbf{x}}_{1,2}(t' - t) + \dot{X}_{\perp}(\mathbb{T}(t', \mathbf{x}_{1,2}(t' - t))) \hat{\boldsymbol{\theta}} \right] \cdot \frac{\dot{\mathbf{x}}_{1,2}(t' - t)}{c} dt', \quad (8)$$

where

$$\dot{X}_{\perp}(\mathbb{T}(t, \mathbf{x})) \equiv \frac{d}{dt} X_{\perp}(\mathbb{T}(t, \mathbf{x})) = \frac{dX_{\perp}(\mathbb{T})}{d\mathbb{T}} \frac{d\mathbb{T}(t, \mathbf{x})}{dt} \quad (9)$$

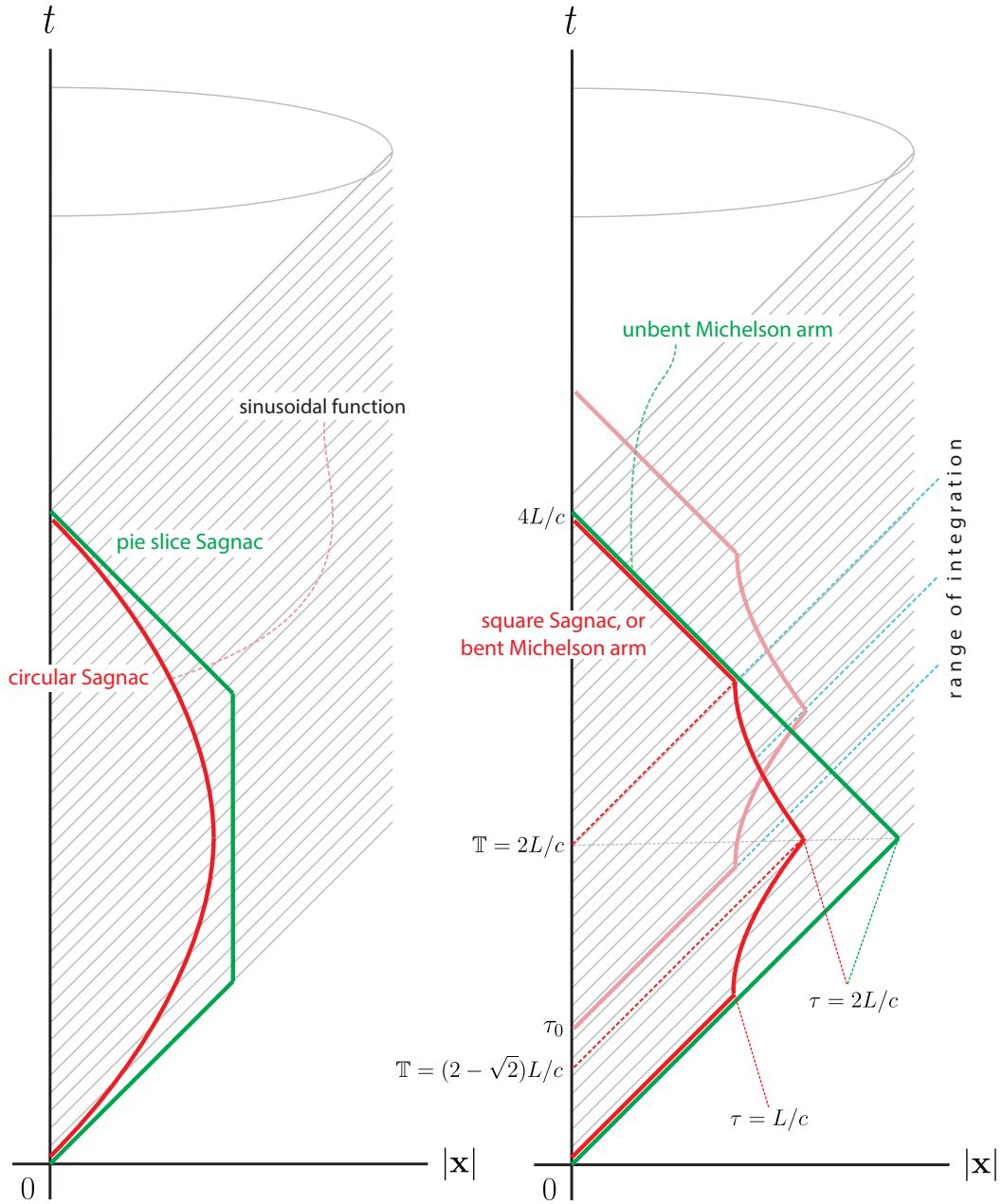


FIG. 2. Space-time diagram showing how quantum twists of the inertial frame project onto an interferometer signal. Laboratory time is plotted against radial position in the observer frame, with the two transverse spatial dimensions suppressed, so each point represents a 2-sphere at a single time. A sequence of future light cones (constant  $\mathbb{T}$  surfaces) is shown for the same observer. Light paths are shown for various interferometer configurations. As a path crosses each light cone, a projection of transverse displacement is added, that accumulates as a random walk and eventually appears as a detectable difference in phase. Note that although the outbound and inbound paths are spatially symmetric in laboratory time, their contribution to exotic correlation is not symmetric in measured signal lag, because the opposite sign for the radial part of their propagation changes the rate at which they cross outbound light cones and thereby accumulate variance. On the right, the red path is shown at two different beamsplitter reflection times, along with the corresponding range of integration for time lag  $\tau_0$ .

is the rate of transverse exotic displacement per propagation time. These displacements occur in the direction transverse to radial separation from the observer's world line, a unit vector in the interferometer plane we denote by  $\hat{\theta}$ . The vector sum of this rate and the classical velocity corresponds to the "effective" velocity of the tracer photon relative to the classical spatial coordinates. The instantaneous effect on the OPL is obtained by taking the component of this effective velocity in the direction of light travel.

Under the variable substitution  $\tau \equiv t' - t$ , eq. 8 becomes

$$S_{1,2}(t + \mathcal{T}) = \int_0^{\mathcal{T}} \left[ \dot{\mathbf{x}}_{1,2}(\tau) + \dot{X}_{\perp}(\mathbb{T}(t + \tau, \mathbf{x}_{1,2}(\tau))) \hat{\boldsymbol{\theta}} \right] \cdot \frac{\dot{\mathbf{x}}_{1,2}(\tau)}{c} d\tau \quad (10)$$

$$= \int_0^{\mathcal{T}} \left[ \dot{\mathbf{x}}_{1,2}(\tau) + \frac{dX_{\perp}(\mathbb{T})}{d\mathbb{T}} \frac{d\mathbb{T}}{d\tau}(\tau, \mathbf{x}_{1,2}(\tau)) \hat{\boldsymbol{\theta}} \right] \cdot \frac{\dot{\mathbf{x}}_{1,2}(\tau)}{c} d\tau \quad (11)$$

$$= c\mathcal{T} + \int_0^{\mathcal{T}} \frac{dX_{\perp}(\mathbb{T})}{d\mathbb{T}} \mathcal{P}_{1,2}(\tau) d\tau \quad (12)$$

Here we use the fact that  $d\mathbb{T}/dt' = d\mathbb{T}/d\tau$  and independent of  $t$ , referring to the definition in eq. 1, and define

$$\mathcal{P}_{1,2}(\tau) \equiv \left[ \frac{d\mathbb{T}}{d\tau}(\tau, \mathbf{x}_{1,2}(\tau)) \right] \left[ \hat{\boldsymbol{\theta}} \cdot \frac{\dot{\mathbf{x}}_{1,2}(\tau)}{c} \right] \quad (13)$$

$$= \left( 1 - \frac{1}{c} \frac{d|\mathbf{x}_{1,2}|}{d\tau} \right) \left( \hat{\boldsymbol{\theta}} \cdot \frac{1}{c} \frac{d\mathbf{x}_{1,2}}{d\tau} \right) \quad (14)$$

$$= \left( 1 - \frac{v_r}{c} \right)_{1,2} \left( \frac{v_{\theta}}{c} \right)_{1,2} \quad (15)$$

as a projection factor that captures all the dependence on the light path of a specific interferometer configuration. The meaning of this factor becomes conceptually clear when we write  $\mathbf{x} = (r, \theta, z)$  in polar coordinates, and denote  $\dot{\mathbf{x}} = (\dot{r}, r\dot{\theta}, \dot{z}) = (v_r, v_{\theta}, v_z)$ . The first half,  $d\mathbb{T}/d\tau$ , is the rate of spacetime propagation relative to outgoing radial null surfaces ( $r/ct = 1$ ), or equivalently, the number of independently fluctuating light cones that the light path slices through per propagation time (see Figure 2). Its value is 0 when the propagation is purely radial in the outgoing direction, 1 when it is purely angular, and 2 when it is purely radial in the incoming direction. This part is a projection in the 1+1D space of  $(t, r)$ . On the other hand, the second half,  $\hat{\boldsymbol{\theta}} \cdot \dot{\mathbf{x}}/c$ , is a projection in the 2D space of  $(r, \theta)$ . It is simply the component of the exotic displacement that is spatially tangential to the light path.

In this form, the spatial fluctuations accumulated over a measurement duration can be clearly seen to manifest as a deviation from the classical OPL. The difference of optical distances along two paths then yields the exotic effect on the OPD,

$$S(t + \mathcal{T}) = \int_0^{\mathcal{T}} \frac{dX_{\perp}}{d\mathbb{T}}(\mathbb{T}(t + \tau, \mathbf{x}_2(\tau))) \mathcal{P}_2(\tau) d\tau - \int_0^{\mathcal{T}} \frac{dX_{\perp}}{d\mathbb{T}}(\mathbb{T}(t + \tau, \mathbf{x}_1(\tau))) \mathcal{P}_1(\tau) d\tau \quad (16)$$

The geometrical projection factor  $\mathcal{P}_{1,2}(\tau)$  determines the statistical response of an instrument of arbitrary geometry.

## B. Single-Interferometer Statistics

Eq. 16 represents OPD measurements made over an interval of time as a set of random variables indexed by measurement time  $t$ . It is a straightforward, if somewhat complicated exercise to calculate the general statistical moments of this measurement set in the presence of exotic spatial fluctuations.

The expected value of an OPD measurement is

$$\langle S(t) \rangle = \left\langle \sum_a^{1,2} (-1)^a \int_0^{\mathcal{T}} \frac{dX_{\perp}}{d\mathbb{T}}(\mathbb{T}(\tau + (t - \mathcal{T}), \mathbf{x}_a(\tau))) \mathcal{P}_a(\tau) d\tau \right\rangle \quad (17)$$

$$= \sum_a^{1,2} (-1)^a \int_0^{\mathcal{T}} \left\langle \frac{dX_{\perp}(\mathbb{T})}{d\mathbb{T}} \right\rangle \mathcal{P}_a(\tau) d\tau \quad (18)$$

$$= 0, \quad (19)$$

using the additive separability of expectation values. The zero mean of the measurement is seen to be a direct consequence of the zero-mean process generating the spatial fluctuations, independent of the geometry of the apparatus.

The autocovariance of two OPD measurements separated in time by  $\tau_0$  is

$$C_{SS}(\tau_0 | \ell_P) \equiv \langle S(t) S(t + \tau_0) \rangle - \langle S(t) \rangle \langle S(t + \tau_0) \rangle \quad (20)$$

$$= \sum_{a,b}^{1,2} (-1)^{a+b} \left\langle \int_0^{\mathcal{T}} \frac{dX_{\perp}}{d\mathbb{T}}(\mathbb{T}(\tau' + (t - \mathcal{T}), \mathbf{x}_a(\tau'))) \mathcal{P}_a(\tau') d\tau' \right. \\ \left. \times \int_{\tau_0}^{\mathcal{T}+\tau_0} \frac{dX_{\perp}}{d\mathbb{T}}(\mathbb{T}(\tau'' + (t - \mathcal{T}), \mathbf{x}_b(\tau'' - \tau_0))) \mathcal{P}_b(\tau'' - \tau_0) d\tau'' \right\rangle \quad (21)$$

$$= \sum_{a,b}^{1,2} (-1)^{a+b} \int_0^{\mathcal{T}} d\tau' \mathcal{P}_a(\tau') \int_{\tau_0}^{\mathcal{T}+\tau_0} d\tau'' \mathcal{P}_b(\tau'' - \tau_0) \\ \times \left\langle \frac{dX_{\perp}}{d\mathbb{T}}(\mathbb{T}(\tau', \mathbf{x}_a(\tau'))) \frac{dX_{\perp}}{d\mathbb{T}}(\mathbb{T}(\tau'', \mathbf{x}_b(\tau'' - \tau_0))) \right\rangle \quad (22)$$

$$= \sum_{a,b}^{1,2} (-1)^{a+b} \int_0^{\mathcal{T}} d\tau' \frac{d\mathbb{T}}{d\tau'}(\tau', \mathbf{x}_a(\tau')) \Theta_a(\tau') \int_{\tau_0}^{\mathcal{T}+\tau_0} d\tau'' \frac{d\mathbb{T}}{d\tau''}(\tau'', \mathbf{x}_b(\tau'' - \tau_0)) \Theta_b(\tau'' - \tau_0) \\ \times \left\langle \frac{dX_{\perp}}{d\mathbb{T}}(\mathbb{T}(\tau', \mathbf{x}_a(\tau'))) \frac{dX_{\perp}}{d\mathbb{T}}(\mathbb{T}(\tau'', \mathbf{x}_b(\tau'' - \tau_0))) \right\rangle \quad (23)$$

The first step (Eq. 21) follows from the vanishing mean just derived; in the second step, the statistical terms are collected together; and in the third step (Eq. 23), projection factors are separated to reduce the integration to a single light cone time variable. We then take a final step (Eq. 24) that invokes the covariance structure of the displacements. The integral is evaluated only in the Planck-size bins where the covariance is not zero, a criterion that determines an inverse function that maps light cone time onto the laboratory time of the corresponding part of the measured signal:

$$C_{SS}(\tau_0 | \ell_P) \approx \sum_{a,b}^{1,2} (-1)^{a+b} c \ell_P \int_{|\tau_0|}^{\mathcal{T}} \Theta_a(\xi_a(\mathbb{T}, 0)) \Theta_b(\xi_b(\mathbb{T}, |\tau_0|) - |\tau_0|) d\mathbb{T}, \quad (24)$$

where we separate out just the spatial part of the projection factor  $\mathcal{P}_{1,2}(\tau)$  as

$$\Theta_{1,2}(\tau) \equiv \hat{\boldsymbol{\theta}} \cdot \frac{\dot{\mathbf{x}}_{1,2}(\tau)}{c} \quad (25)$$

and  $\xi_{1,2}$  is an inverse function for  $\mathbb{T}(t, \mathbf{x})$  defined such that

$$\tau' = \xi_{1,2}(\mathbb{T}, 0) \quad \text{when} \quad \mathbb{T} = \mathbb{T}(\tau', \mathbf{x}_{1,2}(\tau')) \quad (26)$$

$$\tau'' = \xi_{1,2}(\mathbb{T}, \tau_0) \quad \text{when} \quad \mathbb{T} = \mathbb{T}(\tau'', \mathbf{x}_{1,2}(\tau'' - \tau_0)). \quad (27)$$

The inverse function is well-defined everywhere except when  $\mathbf{x}_{1,2}$  is purely radial in the outgoing direction, where  $\mathbb{T}$  is constant over a null path (everywhere else,  $\mathbb{T}$  is monotonically increasing). However, over those segments,  $\Theta_{1,2} = 0$ , making those parts irrelevant. The last step (Eq. 24) should be a highly accurate approximation mathematically; the Planck scale is almost infinitesimal for practical purposes. However, since we treat the covariance structure  $\langle dX_{\perp}/d\mathbb{T} dX_{\perp}/d\mathbb{T} \rangle$  as providing bins of Planck length width, our spacetime is not continuous but discrete at the Planck scale. Formally the integral picks out a single value of  $\Theta_{1,2}$  for each bin in  $\mathbb{T}$ , instead of treating  $\Theta_{1,2}$  as slowly-varying continuous functions. For nearly or exactly radial propagation, the difference can be important in numerical computations, but these regions are suppressed by near-zero values of  $\Theta_{1,2}$ . The mapping between  $\mathbb{T}$  and  $\tau$  is nonlinear and dependent on  $\mathbf{x}_{1,2}$ , which means that in practice, for a specific interferometer configuration, the range of intervals for  $\tau'$  and  $\tau''$  map nontrivially to an integration over  $\mathbb{T}$ . We show examples of this below.

Equations (21) to (24) specify the effect of Planck scale correlations on the signal of any interferometer. In general, the covariance does not vanish but behaves approximately like a Planck random walk for some intervals of time, for a layout where the light paths have a projected transverse component. The autocovariance identically vanishes for separations  $|\tau_0|$  larger than the duration over which an individual measurement has nonzero geometrical projection  $\mathcal{P}_{1,2}(\tau)$  (see Figure 2).

Under the Wiener-Khinchin theorem, an equivalent, frequency-space representation of the autocovariance is the power spectral density (PSD). The PSD is defined as the Fourier transform of the autocovariance,

$$\widetilde{C_{SS}}(f | \ell_P) \equiv 2 \int_{-\infty}^{\infty} C_{SS}(\tau_0 | \ell_P) e^{-i2\pi f \tau_0} d\tau_0 \quad (28)$$

$$= 4 \int_0^{\infty} C_{SS}(\tau_0 | \ell_P) \cos(2\pi f \tau_0) d\tau_0, \quad (29)$$



where the second equality follows from the fact that  $C_{SS}(\tau_0 | \ell_P) = C_{SS}(-\tau_0 | \ell_P)$ . This PSD, written in the so-called engineering convention, is defined only for positive frequencies, in which the power contained in the redundant negative frequencies is folded via the multiplicative prefactor of two.

#### IV. PROJECTIONS FOR EXPERIMENTAL LAYOUTS

To aid in conceptual design of experiments, and to gain insight into the character of the exotic correlations, it is useful to survey the signal response of specific interferometer configurations (see Figure 3). Two features stand out as required for detectable effect: (1) a layout where light travels a substantial distance in a direction that is not purely radial with respect to the “observer” (that is, the beamsplitter whose position defines the measured path difference); and (2) the ability to measure correlations on a timescale short compared with a light travel time in the interferometer arms, or equivalently over a frequency bandwidth comparable to the free spectral range.

The calculational framework above is designed for two optical paths labeled by 1 and 2 that eventually recombine. In the Michelson configurations, a beamsplitter sends light into two separate arms. In the Sagnac configurations[17, 18], the split light travels in opposite directions around the same path. In a Sagnac system, we consider tracer photons propagating in opposite directions and label their optical paths by 1 and 2. The formalism applies entirely unchanged in both cases. Idealized configurations, the “pie slice Sagnac” and the “circular Sagnac,” have curved light paths that can be considered as limiting cases of many short segments. They are presented as thought experiments to demonstrate statistical characteristics of the covariance structure. More realistic configurations for experimental setups are a “square Sagnac” and a “bent Michelson.” One form of the latter will be the main focus of the second phase of the Holometer program, as it is technologically simpler to implement and allows a reliable null configuration.

Throughout this section, we present our spectra normalized with respect to a system timescale  $\mathcal{T}_0$ . This is sometimes the same as light circulation time  $\mathcal{T}$ , but often, because the light phase is not sensitive to rotational shifts when its propagation is purely radial, the effective optical path length over which there is nonzero geometrical coupling is smaller.  $\mathcal{T}_0$  is the duration of time a tracer photon spends within these segments— for example, for the bent Michelson configuration,  $\mathcal{T}_0$  is round trip time within the bent portion of the arm, whereas  $\mathcal{T}$  is the total round trip time.

##### A. Michelson Interferometer with Straight Arms

A standard Michelson interferometer, commonly used in gravitational wave observatories and in the initial phase of the Holometer experiment, has no sensitivity to the exotic rotational effect, due to the fact that the light propagation is always radial with respect to the reference observer world line at the beamsplitter, so that the geometrical coupling  $\Theta(\tau)$  vanishes over the whole light path. Some spatial element of angular propagation is necessary to have nonzero response. This property provides a useful way to design a null experiment to calibrate environmental noise and systematic errors.

##### B. Pie Slice Sagnac Interferometer

This is the simplest configuration to understand, with a perfectly linear time-domain spectrum that is conceptually straightforward to derive. As shown in Figure 3, it consists of two purely radial segments of equal length  $R$ , both of them with zero geometrical coupling  $\Theta(\tau)$  to rotational jitter, connected by a circular arc that spans a quarter circle of radius  $R$ , over which the light propagation is purely angular and the projection factors  $\mathcal{P}_{1,2}(\tau)$  take values of  $\pm 1$ . The completed loop therefore has a system timescale of just  $\mathcal{T}_0 = \frac{1}{2}\pi R/c$  (despite the light circulation time being  $\mathcal{T} = (\frac{1}{2}\pi + 2)R/c$ ), and the total accumulated correlation as a function of time lag  $\tau_0$  is:

$$C_{SS}(\tau_0 | \ell_P) = \begin{cases} 2^2 c \ell_P \mathcal{T}_0 (1 - |\tau_0|/\mathcal{T}_0), & 0 < |\tau_0| < \mathcal{T}_0 \\ 0, & \text{otherwise} \end{cases} \quad (30)$$

where the factor of 2 comes from the two optical paths each picking up the same jitter. The time-domain signal is an autocovariance of the OPD fluctuations, so the factor is squared (see Eq. 21). As the time lag  $\tau_0$  increases in magnitude, the duration of beamsplitter light cone time  $\mathbb{T}$  over which there are correlated fluctuations decreases linearly, up to the total timespan  $\mathcal{T}_0$  over which the light propagation is angular and the light phase is sensitive to rotational shifts.

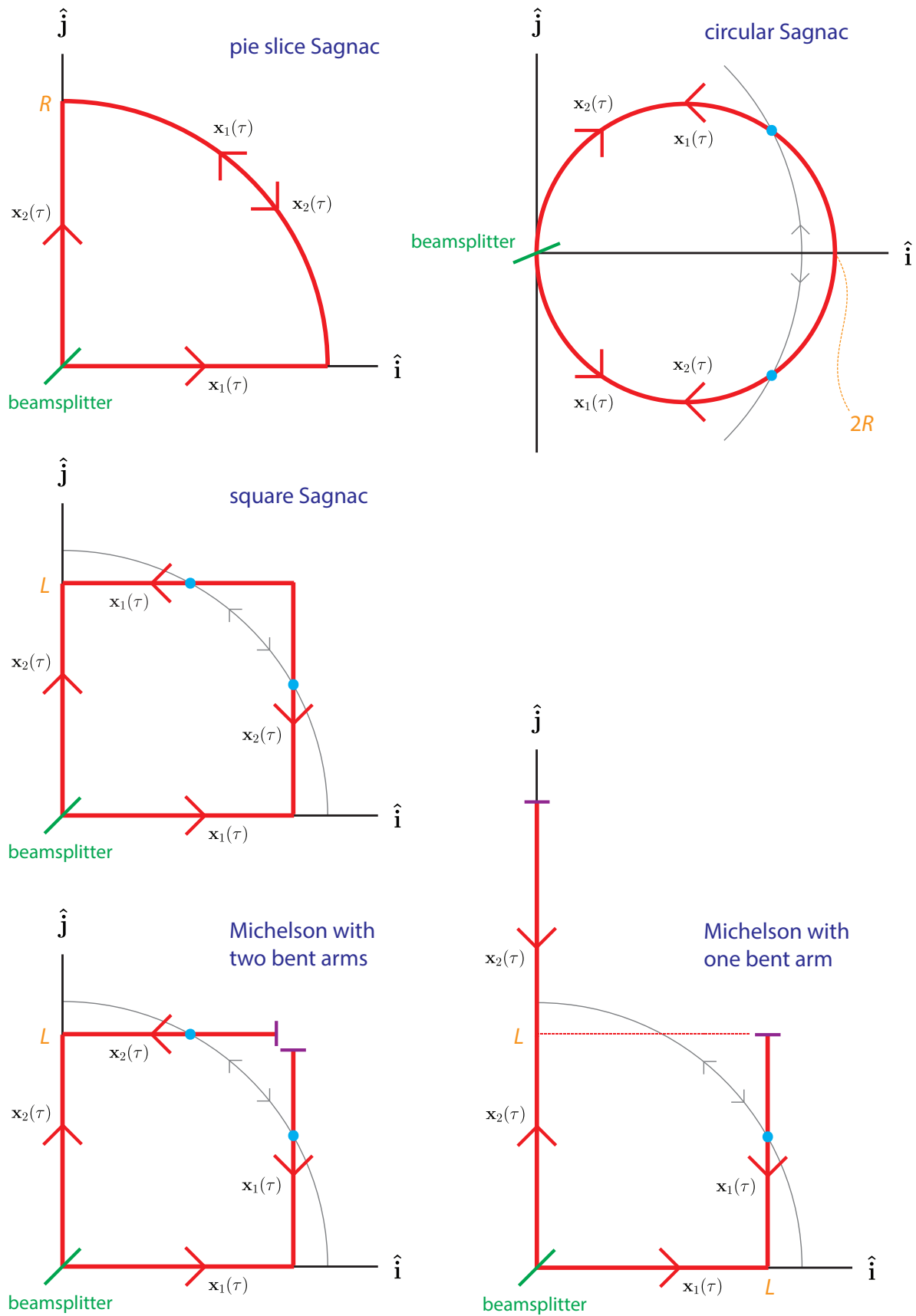


FIG. 3. Schematics of the optical paths in various interferometer setups where the light phase is sensitive to exotic rotation.

The frequency-domain PSD can easily be calculated analytically:

$$\widetilde{C}_{SS}(f | \ell_P) = 8 c \ell_P \mathcal{T}_0^2 \text{sinc}^2(\pi f \mathcal{T}_0) \quad (31)$$

The resulting spectrum is shown in Figure 4. This simple model also gives a fairly close approximation to the exotic noise spectrum in the Sagnac mode[19] of a triangular interferometer, such as LISA.

### C. Circular Sagnac Interferometer

Consider now an idealized Sagnac, a circular loop of radius  $R$  with two light paths going around it in opposite directions, this time starting from a beamsplitter on the circumference. The geometrical coupling  $\Theta(\tau)$  over the light path is a perfect sinusoidal function with one single frequency, at a system timescale equal to light circulation time  $\mathcal{T}_0 = \mathcal{T} = 2\pi R/c$ . The two optical paths can be parameterized as follows (in polar coordinates,  $\mathbf{x} = (r, \theta)$ ):

$$\mathbf{x}_a(\tau) = \left( \frac{c\mathcal{T}_0}{\pi} \sin \frac{\pi\tau}{\mathcal{T}_0}, \pi(-1)^a \left( \frac{1}{2} - \frac{\tau}{\mathcal{T}_0} \right) \right) \quad (32)$$

where  $a = 1, 2$ . We then calculate:

$$\Theta_a(\tau) = \hat{\boldsymbol{\theta}} \cdot \frac{\dot{\mathbf{x}}_a(\tau)}{c} = (-1)^{a-1} \sin \frac{\pi\tau}{\mathcal{T}_0} \quad (33)$$

$$\mathbb{T}(\tau', \mathbf{x}_{1,2}(\tau)) = \tau' - \frac{\mathcal{T}_0}{\pi} \sin \frac{\pi\tau}{\mathcal{T}_0} \quad (34)$$

and similar for  $\tau''$ , with  $\tau = \tau'' - \tau_0$  used as the input. The inverse functions  $\xi_{1,2}(\mathbb{T}, \tau_0)$  are well-defined over the entire domain, but not in analytical form. The integrals for  $C_{SS}(\tau_0 | \ell_P)$  and  $\widetilde{C}_{SS}(f | \ell_P)$  can also only be evaluated numerically. The results are shown in Figure 4.

Notably, despite the perfectly symmetrical and sinusoidal form of the geometrical coupling, the nonlinear mapping between  $\mathbb{T}$  and  $\tau$  in eq. 34 results in an asymmetric weighting over the light circulation time, because there is more accumulated fluctuation when the light path slices through more layers of future light cones per time. This asymmetric response might seem counterintuitive, but it is an important feature of the theory that is a natural consequence of the arrow of time associated with quantum measurement (see section VIB). If one naively assumes a covariance structure that is linearly dependent on  $\tau$  instead of defining  $\mathbb{T}$  on future light cones, the resulting PSD goes negative at certain frequencies, which means that it cannot represent a real-valued physical observable undergoing a wide-sense stationary random process[20].

### D. Square Sagnac Interferometer

The calculations for the device response and spectra expected in a square Sagnac closely follow those of a configuration to be discussed in the next section, a Michelson interferometer with one or two arms bent  $90^\circ$  inward at the midpoint (see Figure 3). Since we are positing a Planckian jitter that is stochastic and covariant on light cones, the magnitude of the total accumulated correlated fluctuation per optical path (1 or 2) is exactly the same for Sagnac and Michelson layouts at zero time lag  $\tau_0$ , despite the difference of a round trip versus a complete loop. The mapping between  $\mathbb{T}$  and  $\tau$  is also identical (see Figure 2). The geometrical coupling  $\Theta(\tau)$  differs by a sign change halfway along the light path, which does significantly change the behavior of the cross correlation at nonzero time lag and thereby the distribution of fluctuation power in the frequency domain. The resulting  $C_{SS}(\tau_0 | \ell_P)$  and  $\widetilde{C}_{SS}(f | \ell_P)$  are shown in Figure 4.

### E. Bent Michelson Interferometer

It is easy to see the schematic similarities between a square Sagnac interferometer and a Michelson with both arms folded inward to form a square. The key difference is whether the light makes complete loops around the square or reflects back halfway through the light path. For the classical Sagnac effect, as in classical rotations measured with optical gyroscopes, this difference matters, because the time-symmetric round trip light path within a bent Michelson

would show zero coupling to that effect. But the exotic rotational fluctuations are stochastic in time and follow the same covariance structures defined on concentric future light cones around an observer at the beamsplitter, so they accumulate total variance at exactly the same rate in both devices, although that variance is distributed differently in measured time and frequency.

Sagnac interferometers are routinely operated as optical gyroscopes, but not with the sensitivity required at high frequency to measure exotic rotational correlations. For technical reasons, the Holometer program plans instead to search for exotic rotational correlations with a pair of Michelson interferometers with only one bent arm. We describe this set up in more explicit detail than the other examples. We also evaluate the displayed solution for definite physical dimensions that approximate the real apparatus. One “north” arm is  $2L = 39$  meters long, and the other “east” arm is bent in the middle with a folding mirror at  $L = 19.5$  meters from the beamsplitter. The reference design is shown in Fig. 3. Since the straight arm has zero coupling to the effect, this device has  $1/2^2$  the amount of accumulated variance observable in a Michelson with two bent arms.

Define unit vectors  $\hat{\mathbf{i}}, \hat{\mathbf{j}}$  in the east and north directions respectively. Adopting a beamsplitter-centered coordinate system, the classical round-trip light paths through the east and north arms can be parameterized as

$$\mathbf{x}_1(\tau) = \begin{cases} c\tau\hat{\mathbf{i}}, & 0 < \tau < T \\ L\hat{\mathbf{i}} + (c\tau - L)\hat{\mathbf{j}}, & T < \tau < 2T \\ L\hat{\mathbf{i}} + (3L - c\tau)\hat{\mathbf{j}}, & 2T < \tau < 3T \\ (4L - c\tau)\hat{\mathbf{i}}, & 3T < \tau < 4T \end{cases} \quad \mathbf{x}_2(\tau) = \begin{cases} c\tau\hat{\mathbf{j}}, & 0 < \tau < 2T \\ (4L - c\tau)\hat{\mathbf{j}}, & 2T < \tau < 4T \end{cases} \quad (35)$$

where  $T = L/c$  and the arm-segment length  $L = 19.5\text{m}$ . It is straightforward to calculate the geometrical couplings:

$$\Theta_1(\tau) = \hat{\boldsymbol{\theta}} \cdot \frac{\dot{\mathbf{x}}_1(\tau)}{c} = \begin{cases} 0, & 0 < \tau < T \\ \Theta_{\rightarrow}(\tau) \equiv \frac{1}{\sqrt{1+(\tau/T-1)^2}}, & T < \tau < 2T \\ \Theta_{\leftarrow}(\tau) \equiv -\frac{1}{\sqrt{1+(3-\tau/T)^2}}, & 2T < \tau < 3T \\ 0, & 3T < \tau < 4T \end{cases} \quad (36)$$

$$\Theta_2(\tau) = \hat{\boldsymbol{\theta}} \cdot \frac{\dot{\mathbf{x}}_2(\tau)}{c} = 0 \quad (37)$$

where we see that the system timescale over which the light phase is sensitive to rotational shifts is actually  $\mathcal{T}_0 = 2L/c$ , instead of the light circulation time  $\mathcal{T} = 4L/c$ . Here the arrows label the outgoing and incoming halves of the light round trip within the bent portion of the arm (the negative sign on the return half of eq. 36 is the only difference we have with the square Sagnac calculations, because there the light completes the loop in one direction).

We also derive the mapping between propagation time and beamsplitter light cone time in the bent “east” arm, shown in Figure 2:

$$\mathbb{T}(\tau'', \mathbf{x}_1(\tau'' - \tau_0)) = \begin{cases} \tau_0 & 0 < \tau'' - \tau_0 < T \\ \mathbb{T}_{\rightarrow}(\tau'', \tau_0) \equiv \tau'' - \sqrt{T^2 + (\tau'' - \tau_0 - T)^2} & T < \tau'' - \tau_0 < 2T \\ \mathbb{T}_{\leftarrow}(\tau'', \tau_0) \equiv \tau'' - \sqrt{T^2 + (\tau'' - \tau_0 - 3T)^2} & 2T < \tau'' - \tau_0 < 3T \\ \tau_0 + 2(\tau'' - \tau_0 - 2T) & 3T < \tau'' - \tau_0 < 4T \end{cases} \quad (38)$$

with a similar expression for  $\tau'$ , with  $\tau_0 = 0$ . These can then be used to evaluate the autocovariance  $C_{SS}(\tau_0 | \ell_P)$  and autospectrum  $\widehat{C}_{SS}(f | \ell_P)$ , from Eqs. (23) and (28). The numerical solution is shown in Fig. 4 for  $\ell_P = l_P$ . A more detailed discussion of the origin of the segmented structure is given in Appendix A.

Interestingly, this spectrum has a nonzero DC response. This might seem counterintuitive, since the light path follows perfectly time-symmetric round trips (unlike in the Sagnac examples): a bent Michelson has no signal response to classical constant rotation. But due to the nonlinear mapping in eq. 38, the outward trip picks up much less jitter than the portion returning inward, when the light path slices through more layers of future light cones per unit time. The fluctuations average to zero, but the device response to exotic twists appears asymmetric. As discussed below (section VIB), this is a consequence of asymmetry between future and past in the preparation of states and decoherence associated with a measurement. Since the frequency spectrum approaches a constant value at zero frequency, the mean square displacement decreases approximately linearly for averaging times longer than the apparatus size, so it goes to zero in the limit of a long time average. The dominant contribution to the total displacement still comes from frequencies on the order of the free spectral range.

With Planck length normalization, the predicted signal is detectable. Assuming sensitivity similar to that already achieved with the Fermilab Holometer[8, 15], a highly significant detection is expected after several hours of integration. With several hundred hours of data, the program should be able to probe an order of magnitude lower.

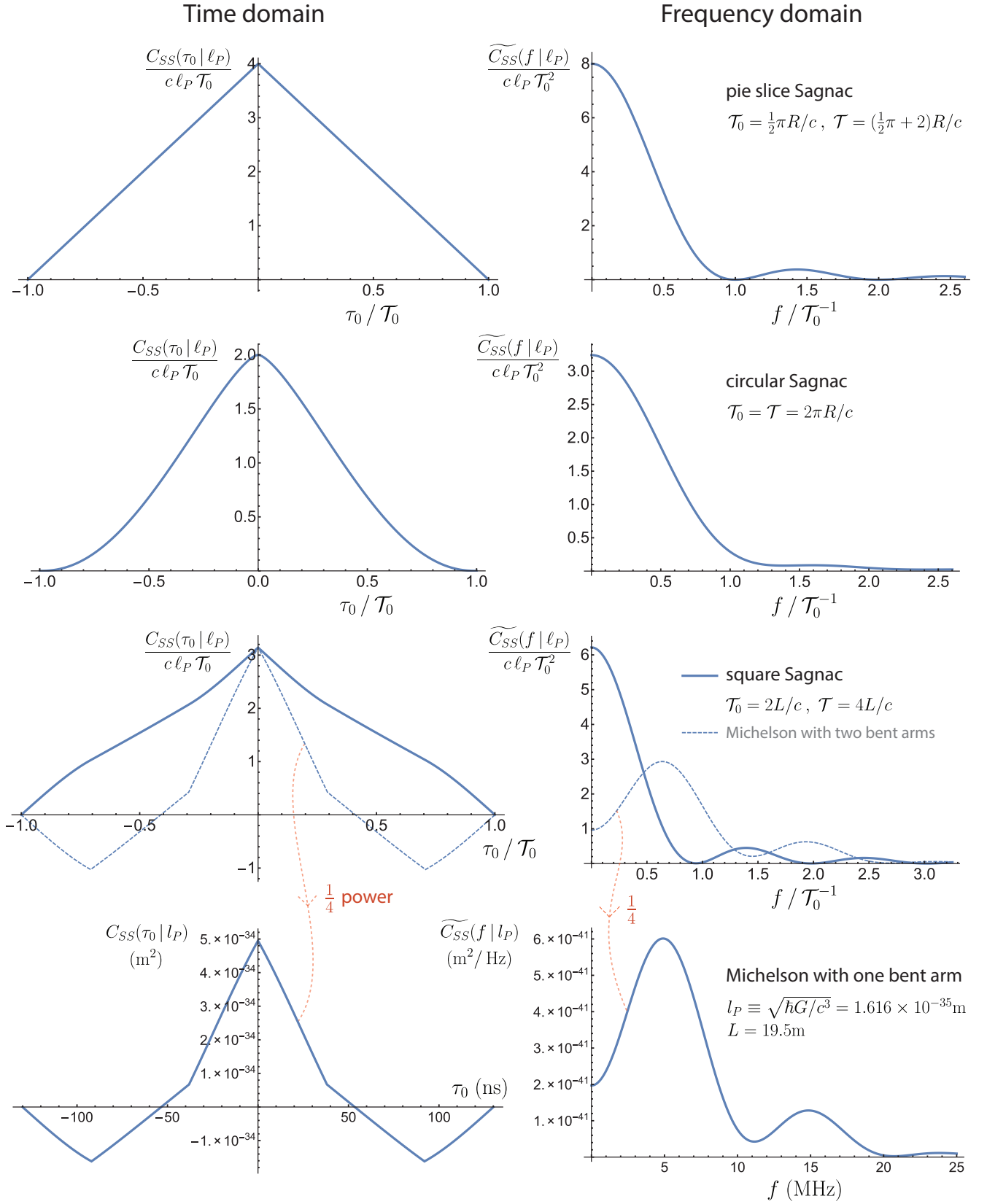


FIG. 4. The time- and frequency-domain autocovariance of signals in various interferometer setups, normalized to their system scales. For the bent Michelson, predictions in physical units are presented, with nominal standard Planck length normalization and the approximate dimensions of an experiment being commissioned. The precise coherence scale is considered a parameter to be fixed by experiment. Note locations of time domain inflections from mirror reflections, as discussed in Appendix A. In the square Sagnac, they occur in the second derivative.

## V. SPATIAL ENTANGLEMENT AND CROSS-CORRELATION

Consider a collection of tangent 2-spheres with a variety of different radii. They represent 2-sections of light cones corresponding to a variety of different observers' world lines. According to the future-light-cone covariance hypothesis, these spheres all share the same exotic phase displacement in the tangent directions, and must "choose" the same value of  $\delta X_{\perp}$  to collapse the Planck subsystem at their intersection point—the same projection of exotic twist onto any axis. Thus, covariance on causal boundaries appears as a sort of spooky conspiracy among many observers belonging to these light cones. How do the Planck subsystems "know about" their large scale relationships with distant observers?

The answer of course is that the relationship among quantum subsystems is always determined by the preparation and measurement of the whole state. The covariance represents entanglement, which is imposed by the assembly of subsystems into a whole system. The projection of the state is fixed by the world line of an observer. Different observers see different projections, but the whole system collapses in a self consistent way. The system is not exactly classical, but has "spooky" correlations. They appear to be nonlocal, with spacelike separations, but actually rigorously respect causal structure.

Indeed, the basic principle is that "all correlations are local": entanglement of states leads to the same transverse displacements for all events on a line with zero space time interval separation. For one observer, we have expressed this statement in terms of future light cone covariance, but the statement still applies in the case of signals cross correlated between two separate interferometers. Exotic fluctuations measured by nearly co-located interferometers are expected to exhibit a high degree of correlation. The degree of entanglement between spatial positions can be expressed in terms of the covariance structure on light cones.

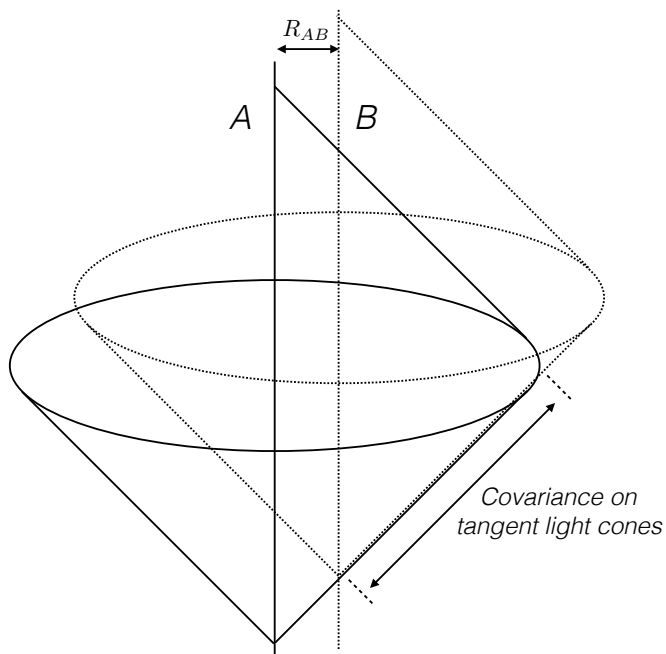


FIG. 5. The entanglement of exotic rotational displacements measured relative to two observers  $A$  and  $B$  is fixed by the in-common future tangent light cones. Along the spatial direction separating the observers, but only at laboratory time separations larger than their separation  $R_{AB}/c$ , exotic displacements for the two are the same. If the  $R_{AB}$  between beamsplitters is small compared to the region explored by their optical paths, signals of two interferometers display significant cross correlation. Thus, exotic rotational fluctuations are highly correlated in both space and time.

Consider the configuration of two observer world lines  $A$  and  $B$ , with separation  $R_{AB}$ , as illustrated in Fig. 5. The displacement rates  $dX_{\perp}^{A,B}/dT_{A,B}$  are relational variables, specific to each observer and its light cone time. Covariance has been defined for future light cones of each observer, but the two sets of displacements are not independent of each other because they share the same emergent space-time. The variables refer to displacements in specific emergent directions in space: projections tangent to the radial vector to each observer. For two observers  $A$  and  $B$ , the directions agree along one line in space, the continuation of the segment separating the observers, where light cones are tangent. Along this line, transverse projections are identical at the same event in the same direction: displacements with

respect to each of the two observers agree in magnitude and direction, for events in their respective future light cones.

This constraint determines the entanglement over the rest of the space-time. The resulting covariance can be written in terms of the two light cone times:

$$\text{cov} \left( \frac{dX_{\perp}^A}{d\mathbb{T}_A}(\mathbb{T}_A), \frac{dX_{\perp}^B}{d\mathbb{T}_B}(\mathbb{T}_B) \right) = \begin{cases} \left( \frac{\ell_P}{t_P} \right)^2, & |\mathbb{T}_A - \mathbb{T}_B| < \frac{1}{2}t_P \\ 0, & \text{otherwise.} \end{cases} \quad (39)$$

Analogously to the single-interferometer case (Eq. 21), the cross-interferometer statistics of two measurement sets can now be calculated by using the covariance in Eq. (39):

$$\begin{aligned} C_{AB}(\tau_0 | \ell_P) &= \langle S_A(t) S_B(t + \tau_0) \rangle \\ &= \sum_{a,b}^{1,2} (-1)^{a+b} \left\langle \int_0^{\mathcal{T}} \frac{dX_{\perp}^A}{d\mathbb{T}_A}(\mathbb{T}_A(\tau' + (t - \mathcal{T}), \mathbf{x}_{A,a}(\tau'))) \mathcal{P}_{A,a}(\tau') d\tau' \right. \\ &\quad \left. \times \int_{\tau_0}^{\mathcal{T}+\tau_0} \frac{dX_{\perp}^B}{d\mathbb{T}_B}(\mathbb{T}_B(\tau'' + (t - \mathcal{T}), \mathbf{x}_{B,b}(\tau'' - \tau_0))) \mathcal{P}_{B,b}(\tau'' - \tau_0) d\tau'' \right\rangle, \end{aligned} \quad (41)$$

where the average is over a time  $t$  in proper time defined by a laboratory clock world line.

Although this formula is almost the same as the autocovariance (Eq. 21), the final result differs from Eq.(24), because the separation  $R_{AB}$  enters implicitly, via the covariance and the range of integration. In laboratory time  $t$ , the agreement  $\mathbb{T}_A = \mathbb{T}_B$  occurs at time offset of  $|t_A - t_B| = R_{AB}/c$ . This slightly modifies the range of integration, which reduces the signal cross covariance below that of the autocovariance.

However, for two similar interferometers separated by a distance much smaller than their size, the non-overlapping parts of the integral due to the time offset are small compared its total value, and the cross covariance is almost equal to the autocovariance. The circle or pie slice examples illustrate this point explicitly. Consider two pie slice interferometers with a small radial displacement offset  $R_{AB} = \delta R \ll R$ . The offset can still be macroscopic, much larger than wavelength, beam width or even mirror size. Since the light cones are almost concentric and the projection factors are geometrically identical except for this fractionally small offset, the nonvanishing part of the correlation integral changes by only a small factor,  $\delta C/C = (C_{AB} - C_A)/C_A \approx -\delta R/R$  (see Fig. 6).

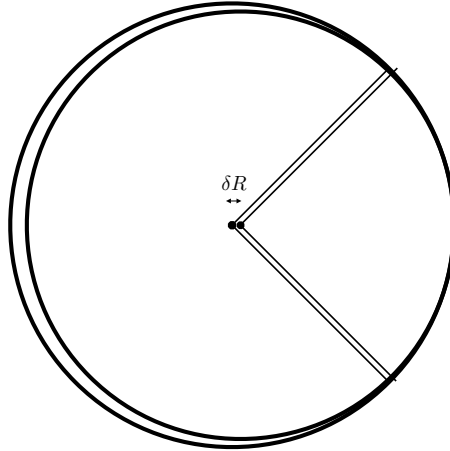


FIG. 6. Slices of two tangent light cone surfaces, with slightly separated centers, at a single time in the lab frame. Because they are tangent, the exotic transverse displacements relative to their respective centers are identical everywhere on both circles. For an offset  $\delta R$  much smaller than the overall scale  $R$ , the integrals that project these displacements onto neighboring pie-slice Sagnac signals (say) differ by only a small fractional amount, of the order of  $\delta R/R$ . Thus, the cross correlation of two machines is close to the autocorrelation, to first order in  $\delta R/R$ , even for macroscopic values of  $\delta R$ . Similarly, it is a good approximation to assume a constant displacement in the plane of the propagating wave fronts or reflecting optics, as long as they are small compared to the scale of the whole system being measured.

Thus, the signals measured by neighboring interferometers correlate in time purely due to the spatial proximity of the instruments, even if their optical paths do not coincide. This behavior makes intuitive sense: they measure the exotic rotation of almost the same emergent space-time volume at almost the same time, in almost the same way.

The exotic displacements on light cones close to the tangent cone are almost the same, because the directions to the beamsplitters at nearly the same and place nearly agree. This property is important in the design of experiments, since it allows them to take advantage of cross correlation to eliminate many spurious sources of noise and signal contamination.

## VI. COMMENTS AND INTERPRETATION

### A. Discrete Qubit Model of Light Cone Twists

The statistical model shows how space-time position relationships can emerge statistically if covariance properties of the random variable  $\delta X_{\perp}$  follow the causal structure defined by an observer's light cones. It is useful to sketch an explicit example that shows how random variables with these covariance properties can emerge from a discrete quantum system. This simple system shows how the intrinsically quantum properties of superposition and collapse or measurement at the Planck scale map onto our classical model. In particular, it shows how the basic assumptions of our statistical model follow from a new physical interpretation of a standard quantum spin system—essentially, exact causal symmetry and statistical Lorentz invariance, recognized by relabeling of coordinates. In this example the quantum system is the same simple two-state qubit widely studied in the literature on quantum computing and entanglement, except for the physical reinterpretation of the quantum observables.

An approximation to a world line emerges from a discrete sequence of events. Each discrete element maps onto a light cone. The light cone in the classical world is 3 dimensional, with 2 space dimensions and one null dimension that corresponds to both time and radial spatial separation in the observer's frame. To represent this 3D system in a discrete quantum system, we adopt displacement operators  $\delta \hat{X}_i$  that obey the standard spin algebra

$$[\delta \hat{X}_i, \delta \hat{X}_j] = i l_P \epsilon_{ijk} \delta \hat{X}_k \quad (42)$$

where  $\epsilon_{ijk}$  denotes the antisymmetric tensor. Algebraically the  $\delta \hat{X}_i$  are exactly equivalent to standard Pauli matrices  $\sigma_i$  used for quantum angular momentum and spin, but expressed in units of Planck length instead of Planck's constant, that is,  $\hbar \rightarrow l_P$ . The eigenvalues for the the standard basis states are then in physical units with modulus  $l_P$ .

A choice of direction to project a light cone state is analogous to choosing an axis to project the state of a spin system. In our application, the radial direction from the observer has a special classical significance, because of its special relationship with emergent time. With no loss of generality, we choose to identify the  $i, j, k = 3$ -axis with the radial direction in the classical correspondence limit, which is also unique the null or time direction of the light cone from a given event, in the observer's frame. This projection is represented by the operator that corresponds to the standard Pauli matrix label  $i, j, k = 3$  or sometimes simply  $Z$ . The other two axes (the conventional Pauli matrix labels  $i, j, k = 1, 2$  or simply  $X, Y$ ) map onto left/right displacements in transverse directions, about each independent classical rotation axis. With these choices, null values for the position observables correspond to the classical inertial frame of the observer, and other values represent deviations from that.

Using standard notation, the state of the system is represented by a vector  $|\psi\rangle$  in a Hilbert space. The basis states along the coordinate axes represent different spatial projections of a two state system: a single qubit of quantum information. For our 2+1 D application we modify the standard notation. We adopt new labels  $|L_1\rangle, |R_1\rangle$  or  $|L_2\rangle, |R_2\rangle$  for the basis states that represent “left” or “right” twists around the  $i, j, k = 1, 2$  axes respectively: these correspond to our exotic transverse displacements. (In quantum computing the  $X, Y$  axis states are commonly labeled  $|+\rangle, |-\rangle$  and  $|+i\rangle, |-i\rangle$  respectively). We adopt new labels  $|\uparrow\rangle, |\downarrow\rangle$  to label the basis states of  $i, j, k = 3$ , the null or radial direction. (These  $Z$  axis state are commonly labeled  $|0\rangle, |1\rangle$ .) The algebra determines how the eigenstates in each projection can be expressed as superpositions of states in the other directions. For example:

$$|\uparrow\rangle = \frac{1}{\sqrt{2}}(|L_1\rangle + |R_1\rangle) = \frac{1}{\sqrt{2}}(|L_2\rangle + |R_2\rangle), \quad |\downarrow\rangle = \frac{1}{\sqrt{2}}(|L_1\rangle - |R_1\rangle) = \frac{1}{\sqrt{2}}(|L_2\rangle - |R_2\rangle) \quad (43)$$

$$|L_1\rangle = \frac{1}{\sqrt{2}}(|\uparrow\rangle + |\downarrow\rangle), \quad |L_2\rangle = \frac{1}{\sqrt{2}}(|\uparrow\rangle - i|\downarrow\rangle). \quad (44)$$

The quantum algebra specifies a relationship among different axes, a property not explicitly addressed in our statistical model. In this system, the axes are independently uncertain, with no “squeezing” from states of one into another. A textbook derivation from Eq. (42) gives independent expressions for transverse displacement operators in a system in a definite  $\delta \hat{X}_3$  eigenstate for the two state system considered here:

$$\langle \delta \hat{X}_1^2 \rangle = l_P^2/2 \quad \text{and} \quad \langle \delta \hat{X}_2^2 \rangle = l_P^2/2. \quad (45)$$



If the symmetries of this quantum model apply in the real world, then the planar statistical model of this paper applies independently in two orthogonal planes, and the variance of classical twists around any axis is given by Eq. (2),  $\langle \delta X_{\perp}^2 \rangle = l_P^2/2$ , as assumed in our model. The expected values of transverse operators also vanish to agree with the classical inertial frame that is used as the coordinate basis, so  $\langle \delta X_{\perp} \rangle = 0$  as assumed in the model.

The serial preparation and measurement of the discrete quantum system creates a time series that approximates a world line in a classical space-time. In the discrete time series, each system element is prepared in an eigenstate of time, which is also the radial direction in space from the observer’s world line. In an actual physical realization, the time sequence does not remain in a superposition of transverse states; because of decoherence, each light cone has to choose whether to turn left or right around each spatial axis at each step. In the Copenhagen version of measurement theory, this process is described as “collapse”, but it can also be regarded as a form of correlation, due to entanglement of the space-time with the observer’s state.

The classical covariance (the spacing in time between the elements, or the “bin width” in Eq. 3) follows from further appeal to the correspondence principle. Each Planck step in proper time along a world line resets the state to the  $|\uparrow\rangle$  or  $|\downarrow\rangle$  eigenstate, which ensures that Planck scale causal symmetry of the light cone states propagates to large scales. The variance in the null direction (the 3-axis of the algebra) maps onto the same value in the classical time and space dimensions, with the standard relationship  $c = l_P/t_P$ , which determines the discrete “timestep”  $\Delta\mathbb{T}$  between light cones:

$$\Delta\mathbb{T}^2 = \langle \delta \hat{X}_3^2 \rangle / 2c^2 = t_P^2/4. \quad (46)$$

Note that no step of this construction has invoked the dynamical postulates of quantum mechanics. The statistical correlations depend only on the more primitive quantum principles that govern Hilbert spaces of states and the operators that represent physical observables, as well as the symmetries of the emergent space-time implicit in our choice of coordinate labels. The physical analysis of the discrete quantum system has invoked superposition, correspondence, and measurement, but no explicit Hamiltonian. Time evolution as in the Schrödinger equation, and the concepts of classical energy, momentum, dynamical conjugate pairings, angular momentum, and indeed  $\hbar$  itself, are all emergent or derived quantities. Thus, the calculation of the effects of these correlations on states of general quantum fields (as opposed to the exactly null-propagating states whose properties depend only on causal structure, and are computed in our model) is highly nontrivial. The correspondence we have used to simplify this calculation only works for one observer world line at a time, since other observers are not perfectly inertial. At the same time, the construction of tangent light cones discussed above shows how a close correlation between nearby observers arises from entangled light cone states.

## B. Time Asymmetry and Decoherence

There is an apparent time asymmetry in the system we have described: the effect on a signal is not the same for outgoing and incoming parts of the same light path. The reason is simple to see: the path encounters light cones at different rates in the two directions. It is also apparent in the correlation functions, which show features at time intervals that do not correspond to the time intervals between reflections.

The asymmetry can be traced to our basic hypothesis of covariance on future and not past light cones. Physically, this choice is motivated by the preparation of the system and matching to the cosmic inertial frame. The “noise” from the Planck scale corresponds to the new information arriving from the past about the rotational frame of the distant universe. A measurement is aligned with the forward direction of time defined by quantum decoherence, which is also the direction in which entropy increases. The “collapse of the wave function” in this situation corresponds to matching with the rotation state of the rest of the universe— the reconciliation of the observer’s state with environmental information, as shown in Fig. 1. It is important to note that all of the measurable predicted correlations, as well as all of the physical elements of the system, are symmetric in time.

## C. Quantum Spookiness and Emergent Time

It seems spooky, in the EPR sense, to say that a space-time itself depends on an observer and a measurement path. But in this sense, a perfectly classical, standard space-time also represents a spooky global conspiracy: the geometry of general relativity is a complete dynamical system that is independent of any observer. Here, a consistent picture emerges if we recognize that there must be spooky (if still causally governed) entanglements among observers. Our model of covariance formulates a specific hypothesis for how macroscopic rotational relationships can emerge statistically from the Planck scale, assuming only a covariance that respects causal relationships. Nested causal

surfaces of the entangled system resemble the intricately interlocked gears of a clockwork (as in Fig. 6.) Tangent displacements at causal boundaries agree at every point for all of the nested causal diamonds at that point. All observers will agree about physical observables, because all exotic “motions,” correlations and projections are defined in terms of radial light propagation and have no effect on radially propagating phase. This consistency also ensures that the whole system closely resembles a continuous classical geometry on large scales. A path in space that begins and ends on an observer’s world line provides an operational statistical definition of an inertial frame, built statistically out of relationships among quantum elements at the Planck scale.

A well known feature of relational quantum geometry is that time itself is also part of the quantum system. This issue has been avoided in the analysis above by analyzing the exotic motion in an observer’s inertial frame, and covariance on Lorentz invariant light cones. For a single world line, light phase along any radial direction represents a perfect “light cone time” clock. But for two separate world lines, their clock phases only agree for light propagating along the radial separation between them. There are differences in the transverse phase, which can be visualized as due an exotic transverse “movement without motion” of the underlying space at each world line relative to the other that causes a Planck scale random drift of transversely oriented light clocks. In this sense, emergent time is not separate from position, but also displays quantum weirdness[1].

To illustrate this point, consider a thought-experiment where the interference in light that travels in the three arms of a triangle are converted into six real signals, which are later combined “in software” as Michelson or Sagnac modes. The exotic correlations should be the same as those computed here, since the correlation structure in our model depends only on classical causal structure. These measurements can be interpreted as comparisons between clocks in different places made in different directions, with exotic spooky correlations caused by departures from inertial frames even of “freely falling” bodies. As seen in the Sagnac and bent Michelson examples above, the total variance imprinted onto a signal around a path is an invariant that depends only on the shape of the path, but the detailed spectrum (the mapping onto an observer’s local time) depends on how and where the signal is evaluated. We can say that the theory is Lorentz invariant, but the projections of states are observer dependent. This thought experiment may some day become actualized in a spaceborne interferometer, although the exotic effect may be buried in gravitational wave foregrounds[19].

#### D. Relation to Emergent Gravity

Our model is based on an empty flat space-time, and does not include any dynamics, matter, or curvature. It can be thought of as special relativity, quantized at the Planck scale— a covariant quantum uncertainty of flat space. On the other hand, because its statistical covariances are built around a generally covariant classical causal structure— that is, light cones and causal diamonds— it provides a natural framework to define rotation, and predict exotic rotational correlations, in emergent theories of gravity.

It has been shown that gravitational dynamics, as described by the Einstein field equations, can be viewed as thermodynamic relationships between entropy, temperature, and heat flux associated with quantum elements at the Planck scale [2–4]. In such a thermodynamic derivation of general relativity, the Einstein equations follow from the requirement that gravitational lensing curves space-time and distorts causal structure by just the right amount for the thermodynamic relations to work. Thermal excitations appear at the macroscopic level as classical gravity, curvature and acceleration. The thermodynamics do not depend on the detailed nature of the quantum elements.

In this view of emergent gravity, our model could be a statistical description of quantum-geometrical fluctuations around a zero temperature ground state— a flat space-time with no matter. The covariance on light cones that defines the measurement and collapse of a space-time state by an observer is associated with the same family of null surfaces that defines thermodynamic quantities. As in thermodynamic gravity, our results do not depend on details of Planck scale quantum elements. At the same time, our model already delves to a deeper level of detail, since it predicts new, observable quantum correlations from the Planck scale that do not exist in the classical theory and have not been predicted in thermodynamic gravity theories. If we adopt Jacobson’s metaphor that general relativity resembles a thermodynamic or hydrodynamic approximation, our model resembles a theory of Brownian motion that reveals specific statistical signatures of atomic components. The metaphor is not exact, because the system in our case is at zero temperature; truly thermal excitations would describe new effects of curvature. General relativity also includes effects of matter degrees of freedom, and their effects on causal structure, that are not included in our model.

In our model of emergent rotation, causal symmetry, Lorentz covariance, and the principle of equivalence are built in— states and displacements live on null surfaces— but directionality and rotation are nonlocally and statistically defined. Locality is in a sense also built into the model, but unlike classical relativity, it is inherited from an observer: distant space displays spooky, exotic, nonlocal spacelike correlations. The principle of equivalence suggests that the model should approximately apply in any empty region of a curved space-time that is sufficiently small (compared to the curvature scale) to approximate a flat space-time, but still much larger than the Planck scale. For example, in a

spinning Kerr black hole, the mean rotation on closed light path much smaller than the hole should almost agree with the spinning “local” inertial frame of the classical metric, but should still display almost the same exotic correlations and fluctuations around this mean value as the same path in flat space. Of course, the same approximation applies very well to interferometer measurements in terrestrial laboratories.

### ACKNOWLEDGMENTS

We are grateful for much encouragement and challenging discussion from other members of the Holometer team. O.K. was supported by the Basic Science Research Program (Grant No. NRF-2016R1D1A1B03934333) of the National Research Foundation of Korea (NRF) funded by the Ministry of Education. This work was supported by the John Templeton Foundation, and by the Department of Energy at Fermilab under Contract No. DE-AC02-07CH11359.

- 
- [1] C. Hogan, Phys. Rev. D (2015), arXiv:1509.07997 [gr-qc].
  - [2] T. Jacobson, Phys. Rev. Lett. **75**, 1260 (1995).
  - [3] E. Verlinde, JHEP **1104**, 029 (2011).
  - [4] T. Padmanabhan, Gen. Rel. Grav. **46**, 1673 (2014), arXiv:1312.3253 [gr-qc].
  - [5] C. Rovelli, *Quantum Gravity* (Cambridge University Press, 2004).
  - [6] T. Thiemann, *Modern Canonical Quantum General Relativity* (Cambridge University Press, 2008) arXiv:gr-qc/0110034 [gr-qc].
  - [7] A. Ashtekar, PoS **QGQGS2011**, 001 (2011), arXiv:1201.4598 [gr-qc].
  - [8] A. Chou, H. Glass, H. Gustafson, C. Hogan, B. Kamai, O. Kwon, R. Lanza, L. McCuller, S. Meyer, J. W. Richardson, C. Stoughton, R. Tomlin, and R. Weiss, Classical and Quantum Gravity **34**, 065005 (2017).
  - [9] C. J. Hogan, Phys. Rev. **D77**, 104031 (2008).
  - [10] C. J. Hogan, Phys. Rev. **D78**, 087501 (2008).
  - [11] C. J. Hogan, Phys. Rev. **D85**, 064007 (2012).
  - [12] C. Hogan, in *9th LISA Symposium*, Astronomical Society of the Pacific Conference Series, Vol. 467, edited by G. Auger, P. Binétruy, and E. Plagnol (2013) p. 17, arXiv:1208.3703 [quant-ph].
  - [13] O. Kwon and C. J. Hogan, Class. Quant. Grav. **33**, 105004 (2016), arXiv:1410.8197 [gr-qc].
  - [14] C. J. Hogan and O. Kwon, Classical and Quantum Gravity **34**, 075006 (2017).
  - [15] A. S. Chou, R. Gustafson, C. Hogan, B. Kamai, O. Kwon, R. Lanza, L. McCuller, S. S. Meyer, J. Richardson, C. Stoughton, R. Tomlin, S. Waldman, and R. Weiss (Holometer Collaboration), Phys. Rev. Lett. **117**, 111102 (2016).
  - [16] R. X. Adhikari, Rev. Mod. Phys. **86**, 121 (2014), arXiv:1305.5188 [gr-qc].
  - [17] E. J. Post, Rev. Mod. Phys. **39**, 475 (1967).
  - [18] K. U. Schreiber, A. Gebauer, H. Igel, J. Wassermann, R. B. Hurst, and J.-P. R. Wells, Comptes Rendus Physique **15**, 859 (2014), the Sagnac effect: 100 years later / L’effet Sagnac : 100 ans après.
  - [19] C. J. Hogan and P. L. Bender, Phys. Rev. **D64**, 062002 (2001), arXiv:astro-ph/0104266 [astro-ph].
  - [20] A. Oppenheim and G. Verghese, *Signals, Systems and Inference, Global Edition* (Pearson Education, Limited, London, UK, 2016).

## Appendix A: Detailed Analysis of the Bent Michelson Configuration

The simple setup of the experiment design chosen for this example allows a detailed set of analytical expressions for the integrals along each segment, as explicitly shown in this appendix. Starting with Eqs. (36) and (37), we see that the light propagation has a nonzero angular component only along the “bent” portion of the east arm. From this point on, we drop the subscripts 1 and 2 for the two arms, and only carry out calculations over the east arm (using  $\mathbf{x}_1(\tau)$  and  $\Theta_1(\tau)$  above). So,

$$C_{SS}(\tau_0 | \ell_P) = \int_0^{4T} d\tau' \frac{d\mathbb{T}}{d\tau'}(\tau', \mathbf{x}(\tau')) \Theta(\tau') \int_{\tau_0}^{4T+\tau_0} d\tau'' \frac{d\mathbb{T}}{d\tau''}(\tau'', \mathbf{x}(\tau'' - \tau_0)) \Theta(\tau'' - \tau_0) \times \left\langle \frac{dX_{\perp}}{d\mathbb{T}}(\mathbb{T}(\tau', \mathbf{x}(\tau'))) \frac{dX_{\perp}}{d\mathbb{T}}(\mathbb{T}(\tau'', \mathbf{x}(\tau'' - \tau_0))) \right\rangle \quad (\text{A1})$$

where  $\mathbf{x}(\tau) = \mathbf{x}_1(\tau)$  and  $\Theta(\tau) = \Theta_1(\tau)$ .

From eq. 38, we derive inverse functions of  $\mathbb{T}_{\rightarrow}(\tau'', \tau_0)$  and  $\mathbb{T}_{\leftarrow}(\tau'', \tau_0)$ , as follows:

$$\tau'' = \xi_{\rightarrow}(\mathbb{T}, \tau_0) \equiv \frac{1}{2} \left( \frac{T^2}{T + \tau_0 - \mathbb{T}} + T + \tau_0 + \mathbb{T} \right) \quad (\text{A2})$$

$$\tau'' = \xi_{\leftarrow}(\mathbb{T}, \tau_0) \equiv \frac{1}{2} \left( \frac{T^2}{3T + \tau_0 - \mathbb{T}} + 3T + \tau_0 + \mathbb{T} \right) \quad (\text{A3})$$

Again, similar equations hold for  $\tau'$ , with  $\tau_0 = 0$ . These inverse functions do not hold over the entire light paths, but in the ranges  $T < \tau' < 3T$  and  $T < \tau'' - \tau_0 < 3T$  where the geometrical coupling is nonzero, they are well-defined.

We use the following notation for the projection factors:

$$\mathcal{P}_{\rightarrow}(\tau) \equiv \left[ \frac{d\mathbb{T}_{\rightarrow}}{d\tau}(\tau, 0) \right] \Theta_{\rightarrow}(\tau) \quad \text{and} \quad \mathcal{P}_{\leftarrow}(\tau) \equiv \left[ \frac{d\mathbb{T}_{\leftarrow}}{d\tau}(\tau, 0) \right] \Theta_{\leftarrow}(\tau) \quad (\text{A4})$$

We now have the tools to evaluate eq. A1, the autocovariance of the signal for a layout that approximates an experiment now under construction.

Evaluating  $C_{SS}(\tau_0 | \ell_P)$  is best done in segments. We know  $C_{SS}(\tau_0 | \ell_P)$  is symmetric, so we will consider positive values of  $\tau_0$  without any loss of generality. Figure 2 is a schematic representation of eq. 38, showing light cone slices of  $\mathbb{T}$  versus the radial axis  $|\mathbf{x}(\tau)|$ , where  $\tau = \tau'$  and  $\tau = \tau'' - \tau_0$  for the two tracer photon trajectories separated by time lag  $\tau_0$ . We see that  $\mathbb{T}(\tau', \mathbf{x}(\tau'))$  or  $\mathbb{T}(\tau'', \mathbf{x}(\tau'' - \tau_0)) - \tau_0$  stays at 0 until the bend mirror ( $\tau = T$ ), runs to  $(2 - \sqrt{2})T$  at the end mirror reflection ( $\tau = 2T$ ), and then to  $2T$  at the bend mirror on the way back ( $\tau = 3T$ ).

Following the covariance structure, the integrals should be performed over the range of time where there are future light cones commonly intersected by both tracer photon paths, within the constraints  $T < \tau' < 3T$  and  $T < \tau'' - \tau_0 < 3T$ . These integrals should be subdivided into separate segments whenever either tracer photon path flips from outgoing to incoming, at  $\tau = 2T$ . Converting the integrals into intervals in  $\mathbb{T}$ , we see that it should be performed between  $\tau_0$  and  $2T$ , with segment divisions at  $(2 - \sqrt{2})T$  and  $\tau_0 + (2 - \sqrt{2})T$ .

Correlations between segments in the same direction (outgoing or incoming) give positive contributions to the integral, but anti-correlations between outgoing and incoming segments give negative ones. This sharp discontinuity in geometrical coupling at the end mirror reflection gives rise to inflections in the autocorrelation whenever a segment division is eliminated by increases in time lag  $\tau_0$  (see Figure 4). This is a feature not seen in the square Sagnac spectra—although the mirror reflections happen at roughly the same points, the geometrical coupling is continuous there.

The functional support for  $C_{SS}(\tau_0 | \ell_P)$  divides into the following three ranges, making clear the origin of these features:

i)  $0 < \tau_0 < (2 - \sqrt{2})T$

$C_{SS}(\tau_0 | \ell_P)$

$$\begin{aligned}
&= \int_{\xi_{\rightarrow}(\tau_0, 0)}^{2T} d\tau' \mathcal{P}_{\rightarrow}(\tau') \int_{T+\tau_0}^{\xi_{\rightarrow}((2-\sqrt{2})T, \tau_0)} d\tau'' \mathcal{P}_{\rightarrow}(\tau'' - \tau_0) \times \left\langle \frac{dX_{\perp}}{d\mathbb{T}}(\mathbb{T}_{\rightarrow}(\tau', 0)) \frac{dX_{\perp}}{d\mathbb{T}}(\mathbb{T}_{\rightarrow}(\tau'', \tau_0)) \right\rangle \\
&+ \int_{2T}^{\xi_{\leftarrow}(\tau_0+(2-\sqrt{2})T, 0)} d\tau' \mathcal{P}_{\leftarrow}(\tau') \int_{\xi_{\leftarrow}((2-\sqrt{2})T, \tau_0)}^{2T+\tau_0} d\tau'' \mathcal{P}_{\rightarrow}(\tau'' - \tau_0) \times \left\langle \frac{dX_{\perp}}{d\mathbb{T}}(\mathbb{T}_{\leftarrow}(\tau', 0)) \frac{dX_{\perp}}{d\mathbb{T}}(\mathbb{T}_{\rightarrow}(\tau'', \tau_0)) \right\rangle \\
&+ \int_{\xi_{\leftarrow}(\tau_0+(2-\sqrt{2})T, 0)}^{3T} d\tau' \mathcal{P}_{\leftarrow}(\tau') \int_{2T+\tau_0}^{\xi_{\leftarrow}(2T, \tau_0)} d\tau'' \mathcal{P}_{\leftarrow}(\tau'' - \tau_0) \times \left\langle \frac{dX_{\perp}}{d\mathbb{T}}(\mathbb{T}_{\leftarrow}(\tau', 0)) \frac{dX_{\perp}}{d\mathbb{T}}(\mathbb{T}_{\leftarrow}(\tau'', \tau_0)) \right\rangle \quad (\text{A5})
\end{aligned}$$

$$\begin{aligned}
&= c \ell_P \int_{\tau_0}^{(2-\sqrt{2})T} \Theta_{\rightarrow}(\xi_{\rightarrow}(\mathbb{T}, 0)) \Theta_{\rightarrow}(\xi_{\rightarrow}(\mathbb{T}, \tau_0) - \tau_0) d\mathbb{T} \\
&+ c \ell_P \int_{(2-\sqrt{2})T}^{\tau_0+(2-\sqrt{2})T} \Theta_{\leftarrow}(\xi_{\leftarrow}(\mathbb{T}, 0)) \Theta_{\rightarrow}(\xi_{\rightarrow}(\mathbb{T}, \tau_0) - \tau_0) d\mathbb{T} \\
&+ c \ell_P \int_{\tau_0+(2-\sqrt{2})T}^{2T} \Theta_{\leftarrow}(\xi_{\leftarrow}(\mathbb{T}, 0)) \Theta_{\leftarrow}(\xi_{\leftarrow}(\mathbb{T}, \tau_0) - \tau_0) d\mathbb{T} \quad (\text{A6})
\end{aligned}$$

ii)  $(2 - \sqrt{2})T < \tau_0 < \sqrt{2}T$

$C_{SS}(\tau_0 | \ell_P)$

$$\begin{aligned}
&= \int_{\xi_{\leftarrow}(\tau_0, 0)}^{\xi_{\leftarrow}(\tau_0+(2-\sqrt{2})T, 0)} d\tau' \mathcal{P}_{\leftarrow}(\tau') \int_{T+\tau_0}^{2T+\tau_0} d\tau'' \mathcal{P}_{\rightarrow}(\tau'' - \tau_0) \times \left\langle \frac{dX_{\perp}}{d\mathbb{T}}(\mathbb{T}_{\leftarrow}(\tau', 0)) \frac{dX_{\perp}}{d\mathbb{T}}(\mathbb{T}_{\rightarrow}(\tau'', \tau_0)) \right\rangle \\
&+ \int_{\xi_{\leftarrow}(\tau_0+(2-\sqrt{2})T, 0)}^{3T} d\tau' \mathcal{P}_{\leftarrow}(\tau') \int_{2T+\tau_0}^{\xi_{\leftarrow}(2T, \tau_0)} d\tau'' \mathcal{P}_{\leftarrow}(\tau'' - \tau_0) \times \left\langle \frac{dX_{\perp}}{d\mathbb{T}}(\mathbb{T}_{\leftarrow}(\tau', 0)) \frac{dX_{\perp}}{d\mathbb{T}}(\mathbb{T}_{\leftarrow}(\tau'', \tau_0)) \right\rangle \quad (\text{A7})
\end{aligned}$$

$$\begin{aligned}
&= c \ell_P \int_{\tau_0}^{\tau_0+(2-\sqrt{2})T} \Theta_{\leftarrow}(\xi_{\leftarrow}(\mathbb{T}, 0)) \Theta_{\rightarrow}(\xi_{\rightarrow}(\mathbb{T}, \tau_0) - \tau_0) d\mathbb{T} \\
&+ c \ell_P \int_{\tau_0+(2-\sqrt{2})T}^{2T} \Theta_{\leftarrow}(\xi_{\leftarrow}(\mathbb{T}, 0)) \Theta_{\leftarrow}(\xi_{\leftarrow}(\mathbb{T}, \tau_0) - \tau_0) d\mathbb{T} \quad (\text{A8})
\end{aligned}$$

iii)  $\sqrt{2}T < \tau_0 < 2T$

$C_{SS}(\tau_0 | \ell_P)$

$$= \int_{\xi_{\leftarrow}(\tau_0, 0)}^{3T} d\tau' \mathcal{P}_{\leftarrow}(\tau') \int_{T+\tau_0}^{\xi_{\leftarrow}(2T, \tau_0)} d\tau'' \mathcal{P}_{\rightarrow}(\tau'' - \tau_0) \times \left\langle \frac{dX_{\perp}}{d\mathbb{T}}(\mathbb{T}_{\leftarrow}(\tau', 0)) \frac{dX_{\perp}}{d\mathbb{T}}(\mathbb{T}_{\rightarrow}(\tau'', \tau_0)) \right\rangle \quad (\text{A9})$$

$$= c \ell_P \int_{\tau_0}^{2T} \Theta_{\leftarrow}(\xi_{\leftarrow}(\mathbb{T}, 0)) \Theta_{\rightarrow}(\xi_{\rightarrow}(\mathbb{T}, \tau_0) - \tau_0) d\mathbb{T} \quad (\text{A10})$$